Journal of Cleaner Production 224 (2019) 384–395

Contents lists available at ScienceDirect

Journal of Cleaner Production

journal homepage: www.elsevier.com/locate/jclepro

(Co-)combustion behaviors and products of spent potlining and textile dyeing sludge

Guang Sun [a, b], Gang Zhang [b], Jingyong Liu [a, *], Wuming Xie [a], Fatih Evrendilek [c, d], Musa Buyukada [e]

[a] Guangzhou Key Laboratory Environmental Catalysis and Pollution Control, Guangdong Key Laboratory of Environmental Catalysis and Health Risk Control, School of Environmental Science and Engineering, Institute of Environmental Health and Pollution Control, Guangdong University of Technology, Guangzhou, 510006, China
[b] Department of Energy and Chemical Engineering, Dongguan University of Technology, Dongguan, 523808, China
[c] Department of Environmental Engineering, Bolu Abant Izzet Baysal University, Bolu, 14052, Turkey
[d] Department of Environmental Engineering, Ardahan University, Ardahan, 75002, Turkey
[e] Department of Chemical Engineering, Bolu Abant Izzet Baysal University, Bolu, 14052, Turkey

ARTICLE INFO

Article history:
Received 12 December 2018
Received in revised form
9 March 2019
Accepted 19 March 2019
Available online 22 March 2019

Keywords:
Spent potlining
Textile dyeing sludge
Thermodynamic analysis
Additives
Ash composition
Gas emission

ABSTRACT

Co-combustion performances, ashes, gases and thermodynamics were quantified for spent potlining (SPL) and textile dyeing sludge (TDS) (with)out CaO. During the four decomposition stages of the blends according to the (D)TG experiments, the interaction among Na, Ca, F, Al, and S led to $CaAl_2O_4$, CaF_2, and Na_2SO_4 which converted inorganic compounds into ash. Increased comprehensive combustion index, and decreased burnout temperature with 50% SPL indicated a better combustion and char burnout, and a shorter combustion process. CaO reduced the F volatilization and increased F^- in the residual ash with 10% CaO. NaF was completely converted into CaF_2 reducing the toxicity of soluble F^- in the residual ash. The predom diagram of Na–Ca–F–S using thermal simulations showed the stable existence regions of CaF_2 and Na_2SO_4. The changed migration mechanisms of F^- and S caused ash compositions to consist of Na_2SO_4 and CaF_2 for the co-combustions, and of NaF and $CaSO_4$ for the mono-combustions. 10% CaO promoted CaF_2, Na_2SO_4, $CaAl_2O_4$, and to a lesser extent, Fe_2O_3. The main gases evolved from the co-combustion included HF, SO_2, COS, CS_2, HCN, NH_3, NO, and NO_2.

1. Introduction

Globally, China is the largest textile producer supplying 40% of world exports (Hasanbeigi and Lynn, 2012). Typically, 200–350 m^3 of pure water is required for one ton of dyed textile products (Liang et al., 2014). Around 2.37×10^9 tons of textile wastewater, and 5.38×10^6 tons of textile dyeing sludge (TDS) with 80% moisture content were generated as the by-product of the textile wastewater treatment plants in China in 2012 (Ning et al., 2014). TDS contains many complex chemical compounds such as perishable organics, pathogens, surfactant, and heavy metals (e. g., Cd, Zn, Cr, and Cu) (Xie et al., 2018a), thus posing a severe threat to the ecosystem health. The dominant sludge disposals were in the form of agricultural applications, landfills, deep-sea dumps, and (co-)combustions. However, the agricultural applications, and landfills are becoming increasingly limited due to the harmful chemical and land occupation impacts of TDS, while sea dumps are banned (Zhang et al., 2013). Among the currently existing methods, high-technology (co-)combustion pathways have come to the forefront since the use of TDS as a feedstock provides energy generation, waste stream reduction, disposal of its toxic components, and by-products such as residual ash as a building material (Cieślik et al., 2015; Kijo-Kleczkowska et al., 2016; Zhuo et al., 2017; Hao et al., 2018a). However, the mono-combustion of TDS is unstable due to its low calorific value and high ash content (Xie et al., 2018a). The TDS co-combustions with a high calorific value feedstock such as energy crops, biomass residues, and coal have been reported not only to achieve a better combustion performance but also to decrease the operational cost and pollutant emissions (Wang et al., 2018a; Xie et al., 2018b).

Globally, about $1–1.5 \times 10^6$ tons of spent potlining (SPL) are annually generated from the aluminum production as a by-product with the high amounts of soluble fluoride (NaF, CaF_2, and Na_3AlF_6),

* Corresponding author.;
E-mail address: Liujy@gdut.edu.cn (J. Liu).

https://doi.org/10.1016/j.jclepro.2019.03.208
0959-6526/

and cyanide (NaCN, $Na_4Fe(CN)_6$, or $Na_3Fe(CN)_6$) (Gao et al., 2016; Sun et al., 2019). Thus, SPL was classified as a hazardous solid waste. When compared to the common treatment methods such as physical separation (Li et al., 2014), and chemical extraction (Birry et al., 2016), the modern (co-)combustion technology is considered an effective method to treat SPL since it reduces the SPL volume, and its toxic content and provides heat owing to its 60% or higher carbon content. It also avoids the disadvantages of the physical separation and chemical extraction methods such as a long leaching time, a low leaching rate, and water pollution (Xiao et al., 2018). SPL was also found to perform well as a secondary fuel in co-firing for the cement plants (Ospina and Hassan, 2017). SPL replacement of coal was reported to reduce coke rates and greenhouse gas emission from the iron-making process (Gao et al., 2016). SPL has a similar carbon content but a higher calorific value (22.21 MJ/kg) than that of coal (14.91 MJ/kg) (Namkung et al., 2018). SPL may be applied as a complementary fuel in the co-combustion with TDS to achieve a higher comprehensive combustion performance.

The high sulfur and fluoride contents of TDS and SPL, respectively, may release air pollutants during their co-combustion due to the interaction among the mineral elements (Zhang et al., 2017). Adsorption is an effective technique for the removal of contaminants, as demonstrated by the use of the fly ash to remove fluoride and phosphate (An et al., 2016). In the industrial sector, CaO has been used as an effective adsorbent to reduce the associated air pollutants from the (co-)combustions such as SO_2, NO_x, CO_2, and F^- as well as to promote the devolatilization (Allen and Hayhurst, 2015; Fernández and Abanades, 2016). The SPL combustion at a high temperature was demonstrated to convert F^- into CaF_2, and then, into residues with the addition of limestone to reduce the emissions of fluoride (Chi et al., 2017; Courbariaux et al., 2004). The addition of CaO, the rich mineral contents (e.g., Fe, Al, Na, Si, and Ca) of SPL and TDS, and the interaction among the minerals can affect the ash deposition and slagging formation during the co-combustion which in turn reduces the heat transfer and combustion performance (Chi et al., 2017). For example, Na combined with (alumino)silicates to form alkali-rich (alumino)silicates was found to influence the surface of deposited ash, and porosity structure at low melting temperatures (Wei et al., 2018; Okoye et al., 2017). Fe and S were separately shown to lead to the formations of Fe_2O_3, and $CaSO_4$ or Na_2SO_4, respectively, in ash in which case $CaSO_4$ plays an important role in slagging at about 1000 °C (Wei et al., 2018). More stable and high-melting temperature inorganic compounds can be formed due to the interaction between SPL and TDS, thus contributing to a complete reaction.

To the best of our knowledge, there is no study about the co-combustion performance, gas evolution and ash deposit formation of TDS and SPL that consider the addition of CaO, and the interaction among S, F^-, and minerals. Therefore, the objectives of this study were to (1) quantify the co-combustion performances of TDS and SPL using non-isothermal thermogravimetric (TG) analyses; (2) identify gas products when CaO was added using TG-mass spectrometric (TG-MS) analyses; (3) determine the mineral phase transformations and elemental distributions of ashes using X-ray Power Diffraction (XRD) and X-ray Fluorescence (XRF) spectrometric analyses, respectively; and (4) thermally simulate the interaction among S, F^-, alkali metals, and ash using FactSage 7.1 software.

2. Materials and methods

2.1. Sample collection and preparation

SPL and TDS were sampled from aluminum smelter and textile dyeing plants in Guangzhou and Foshan of the Guangdong Province in China, respectively. Prior to the start of the experiments, all the samples were air-dried in an oven at 105 ± 1 °C for 24 h, smashed, sieved with a 74-μm sieve and stored in the desiccators for further testing. Physicochemical properties of SPL and TDS were reported in our previous study (Huang et al., 2019; Sun et al., 2019). The mass weight (wt) fractions of TDS in the seven blend ratios of SPL/TDS were set as 0, 50, 60, 70, 80, 90 and 100% and coded thus: SPL, 5/5, 4/6, 3/7, 2/8, 1/9, and TDS, respectively. Also, 3%, 5%, 7% and 10% CaO were added to the 5/5 blend coded as 5/5 + 3% CaO, 5/5 + 5% CaO, 5/5 + 7% CaO, 5/5 + 10% CaO, respectively.

2.2. Experimental design

Thermogravimetric experiments were conducted using a simultaneous DSC-TGA analyzer (NETZSCH STA 409 PC Luxx, Germany) with a detection sensitivity of 0.001 mg. Approximately 6.000 ± 0.500 mg of sample were used in Al_2O_3 crucible for each experiment. The samples were heated from 30 to 1000 °C at 20°C·min^{-1} in the air atmosphere with a flow rate of 50 mL min^{-1}. Initially, several experiments without the samples were performed to obtain the baselines to minimize the instrumental errors. Each experiment was repeated at least three times under the same condition to ensure that errors were within ±2%. TG and derivative TG (DTG) curves were obtained directly from the NETZSCH–T4–Kinetic 2 software.

The ultimate analysis results, and higher heating values (HHV) were determined using an elemental analyzer (Elementary Analysen Systeme Gmbh, Germany) and a Parr 6300 Oxygen Bomb Calorimeter (Parr Instrument Company, United States), respectively. The proximate analysis was performed using a muffle furnace (SX-G12123, China) according to the Chinese criterion "GB/T212-2008". The proximate and ultimate analyses, and HHV (Q_{net}) of SPL and TDS are shown in Table 1.

F^- was determined using an ion selective electrode (ISE, Pinnacle-315P, USA). Na was detected using an atomic absorption spectrophotometer (AAS-240, USA), while Al was determined using the chemical titration method. An inductively coupled plasma optical emission spectrometer (ICP-OES, ICAP7400, Thermo, USA) was used to obtain the compositions of the other minerals. All the results are presented in Table 1.

Crystalline phases were determined using an XRD (MiniFlex 600, Rigaku Corporation, Japan) at a scanning range and velocity of 10–90° and 2°·min^{-1}, respectively. The X-ray tube was performed at 40 kV and 40 mA. The powdered samples were analyzed using Cu Kα radiation (λ = 0.15418 nm) with a step size of 0.02°. The instrumental goniometer reproducibility was 0.0001°. The chemical compositions of the residual ash were measured using a wavelength dispersive XRF spectrometer (WDXRF, AxiosmAX Petro, PANalytical B.V. Corporation, Netherlands). Its test range was 1 ppm, while the instrumental accuracy was less than 0.05%.

The TG-MS spectrometric experiments were carried out using a Thermo Mass Photo TG-DTA-PIMS 410/S (Rigaku Corporation, Tokyo, Japan) with an electron bombardment ionization source. The TG-MS analyses were conducted in the range of 30–1000 °C at a heating rate of 20 °C·min^{-1} in the air atmosphere with a flow rate of 150 mL min^{-1}.

2.3. (Co–)combustion performances

The following five (co-)combustion characteristic parameters were used in this study: (1) peak temperature (T_p), (2) ignition temperature (T_i)—the intersection between the tangent line of the point at which decomposition started and the tangent line of (3) the maximum weight loss rate ($-R_p$), and (4) burnout or final temperature (T_f)—98% of total mass loss, and (5) average weight

Table 1
Physicochemical properties of SPL and TDS (Huang et al., 2019; Sun et al., 2019).

Parameter	SPL	TDS	Chemical matter (*wt%*)	SPL	TDS
Ultimate analysis (wt%)			Na_2O	11.44	3.84
C	69.11	16.62	Al_2O_3	7.58	0.47
H	0.40	3.02	CaO	1.17	5.58
N	0.16	3.33	Fe_2O_3	1.42	35.80
Proximate analysis (wt%)			MgO	0.13	0.84
Moisture	0.73	5.70	K_2O	0.27	0.18
Volatiles	1.56	27.83	SiO_2	2.21	4.33
Fixed carbon	68.67	3.62	P_2O_5	<0.01	1.43
Ash	29.04	62.85	F	10.40	/
Higher heating value (*MJ/kg*)	22.21	6.95	S	0.26	6.82

loss rate ($-R_v$). The parameters were obtained from the (D)TG curves to evaluate the effects of the heating rates on the (co-)combustion performances (Huang et al., 2016). Comprehensive combustibility index (*CCI*) was used to assess the combustion property with the higher *CCI* value indicating a better (co-)combustion property and expressed as follows (Xie et al., 2018a):

$$CCI = \frac{(-R_p) \times (-R_v)}{T_i^2 \times T_f} \quad (1)$$

2.4. Thermodynamic simulations

Thermodynamic equilibriums of the mineral phases were computed using the FactSage 7.1 software based on the theory of Gibbs free energy minimization in a closed system. The input data used were thus: C, H, N, F, S, Na_2O, Al_2O_3, Fe_2O_3, MgO, CaO, K_2O, SiO_2, and P_2O_5 (Table 1). The gas and condensed phases were assumed to be ideal and pure, respectively. The combustion temperature varied between 600 and 1200 °C at an interval of 50 °C, while excess air ratio, and pressure were set to 1.5 and 101.325 kPa, respectively. The predom diagrams of Ca–Na–S–F at 750, 850 and 1000 °C were estimated using the phase diagram of the FactSage software. The melting temperature of residual ashes in the ternary phase diagram systems of $CaO–Na_2O–Al_2O_3$ and $CaO–Fe_2O_3–Al_2O_3$ was calculated using the phase diagram of the FactSage 7.1 software. The amount of melting phase in the residual ash was estimated as a function of increased temperature.

3. Results and discussion

3.1. Mono-combustion performances of SPL and TDS

The (D)TG curves of the mono-combustions in the air atmosphere at 20 °C·min^{-1} are shown in Fig. 1. The DTG (Fig. 1b) curves showed a four-stage mass loss of TDS. The first stage of 30–137.5 °C occurred with the mass loss of 3.42% due to water evaporation. The second stage of 137.5–351.5 °C led to a 17.94% mass loss at a maximum reaction rate of 2.73%·min^{-1} due to the devolatilization of organic matters such as carbohydrates, proteins, and aliphatic (Wang et al., 2018a). The third stage of 351.5–600 °C continued to combust organic matters with stronger bonds such as aromatic compounds (Wang et al., 2018a) and had a mass loss of 12.42% at a maximum reaction rate of 2.19%·min^{-1}. The final stage was due to the decomposition of inorganic minerals such as carbonate, dolomite, kaolin, and fixed carbon (Liang et al., 2014) with a mass loss of 3.51%.

The DTG curves of TDS and SPL significantly differed under the same conditions. The DTG (Fig. 1a) curves pointed to a single-stage decomposition process of SPL between 450 and 800 °C corresponding to the fixed carbon combustion with a mass loss of 60.92%. No peak of mass loss was observed at below 450 °C which can be attributed to the low moisture and volatiles, and the stable inorganic compounds at a lower temperature (such as NaF, $NaAl_{11}O_{17}$, CaF_2, and Na_3AlF_6) of SPL. The final masses of SPL and TDS were estimated at 31.24 and 61.72%, respectively, due to the higher carbon and lower ash contents of SPL than TDS. The peaks of mass loss corresponded to 103.8, 277.1 and 416.7 °C for TDS, and to 599.2 °C for SPL, with their maximum rates of 0.98, 2.73, 2.14 and 8.15%·min^{-1}, respectively.

The (co-)combustion parameter estimates in the air atmosphere at 20 °C·min^{-1} are presented in Table 2. The maximum combustion rate, the peak temperature, and the ignition temperature of TDS were lower than those of SPL. Thus, TDS had higher reactivity due

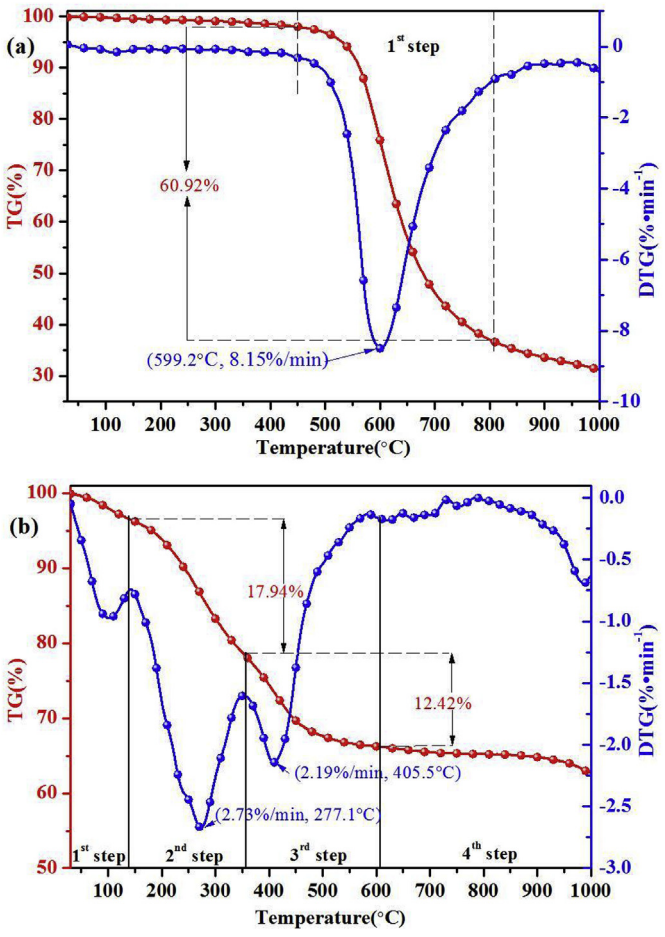

Fig. 1. (D)TG curves of (a) SPL and (b) TDS mono-combustion in the air at 20 °C·min^{-1}.

Table 2
(Co−)combustion parameters of SPL and TDS in the air atmosphere at 20 °C·min^{-1}.

Parameter	SPL	TDS	1/9	2/8	3/7	4/6	5/5
Ignition temperature (T_i, °C)	551.8	215.6	218.6	222.3	227.9	232.5	235.3
Maximum weight loss rate (-R_p, %·min^{-1})	8.15	2.73	2.56	2.22	2.64	3.47	4.24
Peak temperature (T_{p1}, °C)	599.2	277.1	267.7	272.5	279.4	279.1	271.9
Peak temperature (T_{p2}, °C)	/	405.5	415.6	413.5	394.6	401.9	403.6
Peak temperature (T_{p3}, °C)	/	/	656.4	637.4	638.5	660.2	652.5
Average weight loss rate (-R_v, %·min^{-1})	1.42	0.82	0.87	0.92	0.96	1.03	1.13
Final or burnout temperature (T_f, °C)	940.8	977.1	944.8	882.2	863.9	872.6	868.8
Final mass (M_f, %)	31.24	62.72	60.41	57.38	55.18	51.59	46.09
Comprehensive combustion index (CCI, 10^{-8}%^{2}·°C^{-3}·min^{-2})	4.21	4.90	4.92	4.70	5.65	7.55	9.96

to its higher volatiles (27.83%) than SPL (1.56%) (Wang et al., 2018a). The higher *CCI* of TDS than SPL may result from more easily degradable organic matter of TDS than SPL (Fan et al., 2016). However, the higher burnout temperature of TDS than SPL suggested a relatively longer combustion process of TDS than SPL.

The decomposition of $CaSO_4$ in TDS at about 900 °C may contribute to the longer combustion process of TDS than SPL ($CaSO_4$+CO→CaO+SO_2+CO_2) (Tian et al., 2016).

3.2. Co-combustion performances

The co-combustion performances in the air atmosphere at 20 °C·min^{-1} are presented in Fig. 2. The increased final masses (from 47.81 to 60.41%) with the decreased blend ratio (the increased TDS proportion) (Fig. 2a) was attributed to the high ash content of TDS. A rapid mass loss occurred with the increased TDS due to the decomposition of its volatiles at below 600 °C but due to the combustion of fixed carbon in SPL in the range of 600–1000 °C. The four peaks of the blend combustions (Fig. 2b) were similar to those of the mono-combustions. The co-combustion reaction rate rose with the increased TDS at below 550 °C. This suggested that the reaction rate in this stage was controlled by the decomposition of organic matter of TDS such as fiber, protein, and saturated aliphatic chains (Hu et al., 2015). More heat release due to the volatiles decomposition of TDS in turn boosted the combustion process of fixed carbon.

The combustion profile of SPL shifted towards a lower temperature than did that of the blends probably due to the decomposition of fixed carbon, and the release of more heat at above 450 °C. The conversion rates of the co-combustions lay in between the mono-combustion ones at below 750 °C, most likely due to the higher volatiles content of TDS (Fig. 2c). The heat energy associated with the easily and early combusted volatiles raised the system temperature and promoted the further decomposition of volatiles and carbon. The reason for the higher conversion rates of the blends than the individual fuels at above 750 °C may be two-fold: (1) the early combusted volatiles might burn carbon in SPL, thus causing more heat and a high flame temperature to favor the combustion burnout, or (2) the interaction among certain minerals (e.g., Na, Ca, Si, and Al) of the blends might favor the reaction of inorganic compounds, and thus, improve the catalytic influence and stability at > 750 °C.

The lower ignition temperature (T_i) of TDS than SPL indicated an easier ignition and earlier release of more organic matter of TDS than SPL. The elevated ignition temperature with the increased SPL may be explained by the slower devolatilization progress of SPL than TDS. This case was attributed to the decomposition of fixed carbon that required more heat energy and was more difficult than that of organic matter in TDS. The increased SPL (from 10 to 50%) decreased the burnout temperature (T_f) from 944.8 to 868.8 °C and the final mass (M_f) from 60.41 to 46.09%. The high T_f value as an indicator of a long combustion process suggested that the burnout of the blends was delayed with the increased TDS (Wang et al., 2018a). The higher *CCI* of the 5/5 blend than SPL was due to the high combustion burnout and ignition temperatures of SPL (Table 2). The *CCI* rose when TDS decreased from 90 to 50%. The lower T_f values of the blends than the individual fuels pointed to their higher burnout performance. The higher *CCI* and lower T_f value of the 5/5 blend than the lower blend ratios (the higher TDS) may be more favorable in terms of the co-combustion performance (Hao et al., 2018a). Overall, the higher blend ratios were demonstrated to exhibit a better comprehensive combustion performance.

3.3. Interaction between SPL and TDS

To determine the interaction between SPL and TDS, the experimental and theoretical TG/conversion rate (CR) curves were compared. The theoretical TG estimates (TG_{cal}) for the blends were expressed with Eq. (17) thus (Qi et al., 2018):

$$TG_{cal} = x_s(TG)_{SPL} + (1\text{-}x_s)\,(TG)_{TDS} \tag{17}$$

where x_s is the SPL fraction of the blends, $(TG)_{SPL}$ and $(TG)_{TDS}$ were the experimental TG curves of the individual SPL and TDS, respectively. The theoretical CR estimates (CR_{cal}) for the blends were expressed with Eq. (18) thus (Wang et al., 2017):

$$(CR)_{cal} = \frac{x_s M_{SPL} + (1 - x_s)M_{TDS}}{1 - x_s A_{SPL} - (1 - x_s)A_{TDS}} \tag{18}$$

where M_{SPL} and M_{TDS} were the mass losses of SPL and TDS, respectively; A_{SPL} and A_{TDS} were the ash yields of SPL and TDS, respectively. Deviation (%) was introduced to assess the strength of the interactions based on Eq. (19) as follows:

$$\text{Deviation } (\%) = \left(\frac{(TG/DTG)_{exp} - (TG/DTG)_{cal}}{(TG/DTG)_{cal}}\right) \times 100\% \tag{19}$$

The experimental and calculated curves of mass loss were consistent during the decomposition of organic matter at < 450 °C (Fig. 3). The difference between them in the range 450–850 °C suggested a more significant interaction between SPL and TDS in this stage. The reason for this may be related to the fact that the heat release from the early combustion of volatiles in TDS accelerated the endothermic reaction which in turn promoted the late decomposition of carbon in SPL. The interaction between biomass and coal was previously reported to be controlled by the thermal effect (Guo and Zhong, 2018a).

Deviation rose with the increased SPL and peaked (11.31%) with the 5/5 blend at 641.7 °C during which the experimental mass loss lagged behind the calculated one which pointed to some interactions (Li et al., 2018). On the contrast, the calculated mass loss significantly lagged behind the experimental one for the blends

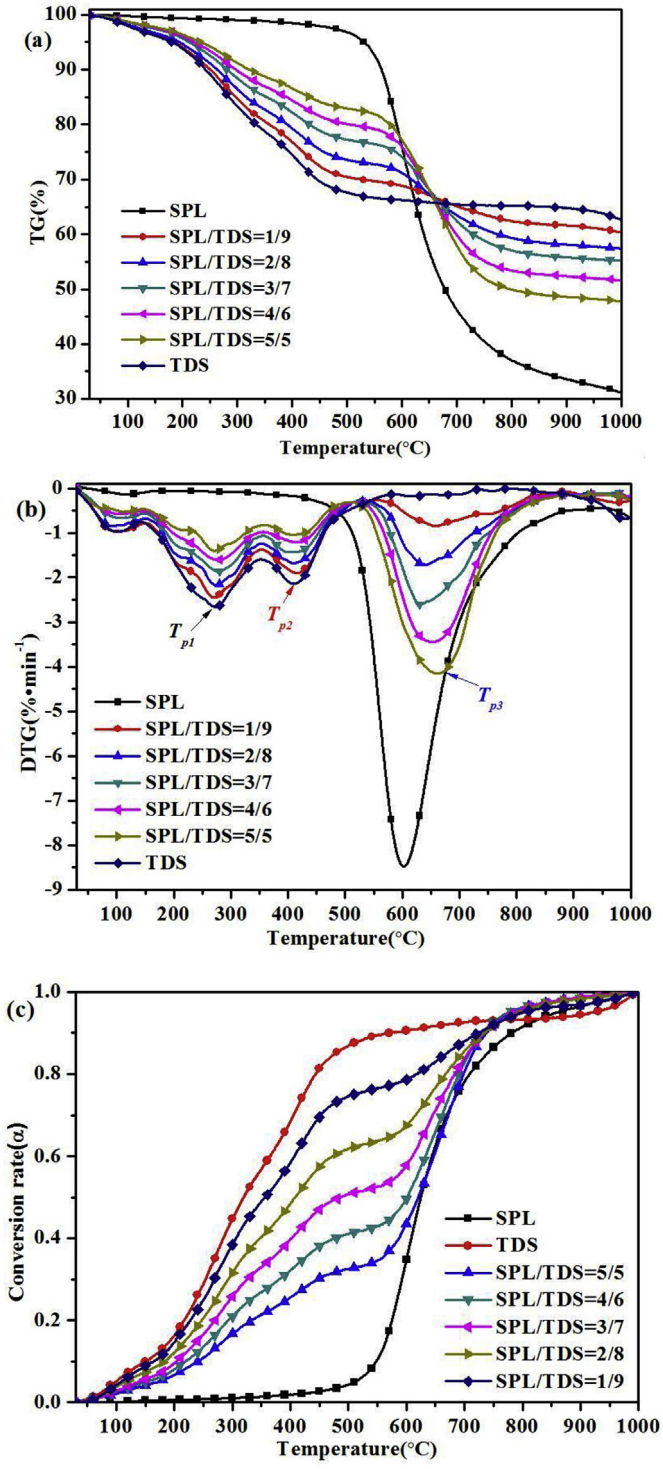

Fig. 2. (a) TG, (b) DTG and (c) conversion rate curves of (co-)combustions in air atmosphere at 20 °C·min^{-1}.

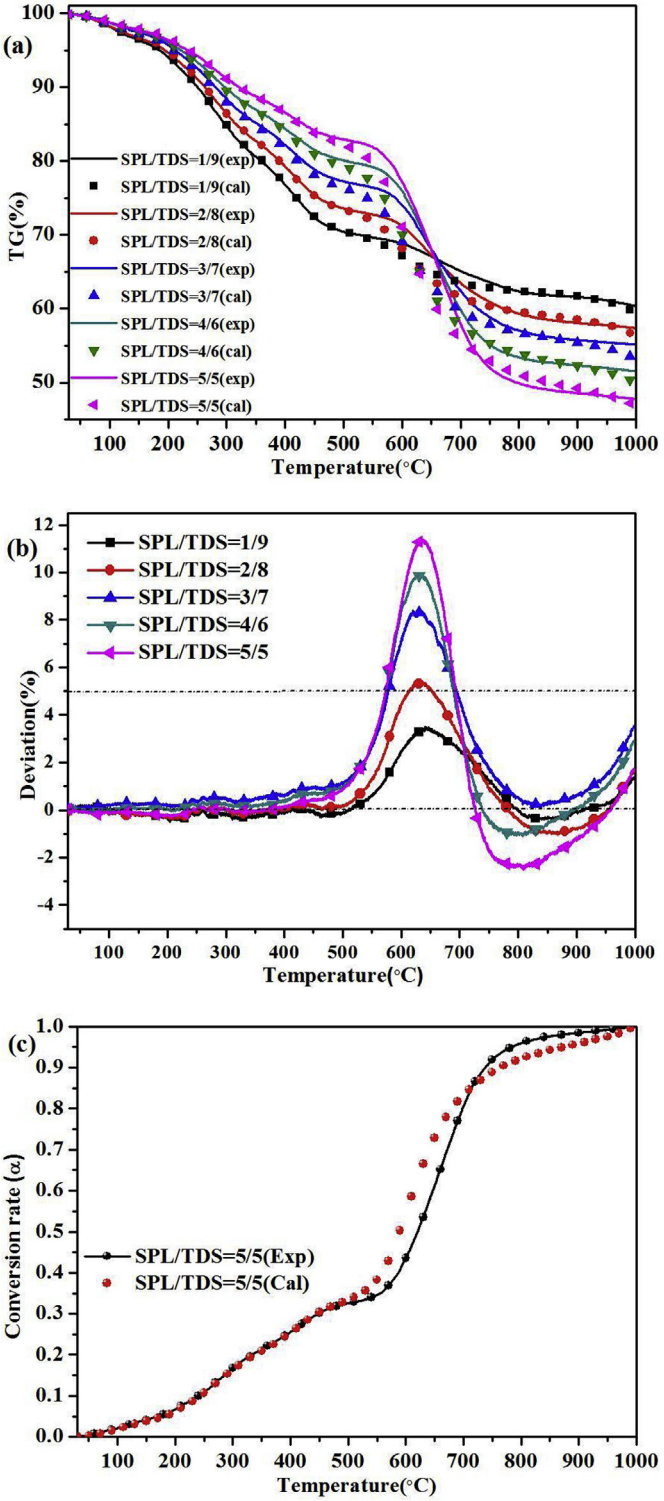

Fig. 3. (a) Experimental and calculated TG curves of the blends, (b) deviation profiles, and (c) experimental and calculated conversion rates of the 5/5 blend in air atmosphere at 20 °C·min^{-1}.

most likely due to the heat release from the combustion of carbon in SPL that increased the mineral interaction rate. The char formation due to the TDS decomposition may have catalyzed the degradation of SPL ash residues such as Fe, Ca, and Si, thus leading to a complete combustion (Xie and Ma, 2013). The conversion rate was not consistent between the experimental and calculated curves at above 450 °C (Fig. 3c), which pointed to some interaction for the blends. Also, the higher experimental conversion degree than the calculated one pointed to the early completion of the reaction. This case was attributed to the interaction among the mineral elements of SPL and TDS, and to the subsequent formation of more stable inorganic compounds. The deviation values were

less than 2% at below 450 °C, thus suggesting no interactions for the blends (Guo and Zhong, 2018b). Overall, some interactions occurred in the range of 450–1000 °C, with the 5/5 blend exhibiting the strongest interaction.

3.4. Effect of CaO additions on co-combustions

In response to the addition of the four CaO ratios to the 5/5 blend, the (D)TG curves in the air atmosphere at 20 °C·min^{-1} showed the similar trends that were divided into the four stages in the ranges of 30–137.5, 137.5 to 500, 500 to 800 and 800–1000 °C (Fig. 4). The peak temperature shifted towards the low temperature with more than 7% but not less than 5% CaO (Fig. 4c–d). Ca was reported to act as an O_2 carrier increasing its reactivity (Niu et al., 2015). Similarly, the increased addition of CaO to the blends in the present study caused O_2 to easily capture free Ca, thus improving the reactivity. The interaction between CaO and the blends made the maximum peak temperature shift towards the low temperature, thus increasing the reaction rates.

The lower T_i and T_f values with the 5/5 + 10% CaO blend (Table 3) indicated an easily occurring ignition and a short combustion time. CaO improved the combustion performance and promoted the maximum reaction rate. The reaction of the low CaO content of the blend with F^- to form CaF_2 weakened the catalytic effect of CaO (Liu et al., 2018a). The increased CaO addition may cause the mineral elements to interact with Ca, thus generating Ca–Al and Ca–Si compounds, which in turn improve the catalytic influence and stability (Wang et al., 2019). CaO may react with CO_2 to form $CaCO_3$ in the range of 650–700 °C. The increased porosity of sample surface due to the decomposition of $CaCO_3$, the formations of $CaSO_3$ and $CaSO_4$ at the high temperature, and the resultant CO_2 emission appeared to enhance the oxygen diffusion, and thus, the combustion properties.

3.5. Residual ashes of mono-combustions without CaO addition

The XRD and XRF analyses were performed for the residual ashes of the individual SPL and TDS, and their elemental retentions and phases (Fig. 5). SPL had the abundant amounts of Na, Al, and F in its residual ash (Fig. 5a). Although Na is very volatile at > 900 °C, the Na retention of SPL was higher at 1000 °C than 850 °C most probably since the Al-rich content of SPL interacted with Na and Al to form $NaAlO_2$, $NaAl_{11}O_{17}$, or $NaAlSiO_4$ ($Na_2O+Al_2O_3=2NaAlO_2$, $Na_2SO_4+2SiO_2+Al_2O_3\rightarrow 2NaAlSiO_4+SO_2+0.5O_2$) (Li and Chen, 2010). Sodium compounds were reported to exist as $NaAlSi_3O_8$ at below 600 °C (Wang et al., 2018c). The decomposition of $NaAlSi_3O_8$ in turn formed the phases of SiO_2, Al_2O_3, and $NaAlO_2$ ($NaAlSi_3O_8\rightarrow SiO_2+Al_2O_3+NaAlO_2$) (Xing et al., 2018). SiO_2 and Al_2O_3 alone were found to have a high melting temperature but to form the low-melting compounds when combined with Na, thus promoting the slagging processing (Moço et al., 2018). This case was illustrated in the XRD pattern of SPL (Fig. 5b) with the clear signals of $NaAlO_2$, $NaAl_{11}O_{17}$, and $NaAlSiO_4$ at 1000 °C. Sodium aluminosilicates were shown to be recalcitrant at higher temperatures being retained in the residual ash (Qi et al., 2018). The Si retention in SPL ash rose with the elevated temperature. The disappearance of the weak signal of Na_3AlF_6 at 1000 °C was consistent with the fact that it was converted into NaF and AlF_3 at 1000 °C ($Na_3AlF_6=AlF_3+3NaF$). AlF_3 further formed CaF_2 in the residual ash due to the higher thermal stability of CaF_2 than AlF_3 ($2A1F_3+3CaO = 3CaF_2+Al_2O_3$) (Li and Chen, 2010). At the higher temperatures, $Na_4[Fe(CN)_6]$ in SPL was converted into Fe_2O_3. ($2Na_4[Fe(CN)_6]+15.5O_2=Fe_2O_3+12CO_2+6N_2+4Na_2O$) can be attributed to the slight Fe_2O_3 signal of the XRD patterns (Fig. 5b). The main phase of the SPL residual ash was controlled by the inorganic compounds of CaF_2 and NaF.

The S content of TDS decreased from 8.85 to 5.61% with the elevated temperature due to its conversion into SO_x. The residual ash yield of Fe dropped from 36.52 to 39.12%. SO_2 absorbed by $CaCO_3$ was shown to form $CaSO_4$ in the range of 600–750 °C with the weak intensity of $CaSO_4$ at 1000 °C ($CaCO_3+SO_2+1/2O_2=CaSO_4+CO_2$) (Liu et al., 2016). The slight change in Ca from 6.54 to 6.28% may be attributed to the weaker $CaSO_4$ and stronger Fe_2O_3 signals (Hao et al., 2018b). Fe_2O_3 was observed as the main species of the TDS combustion due to its Fe-rich content (Fig. 5c). Fe_2O_3 was difficult to decompose and retained in the ash at below 1000 °C (Xing et al., 2018).

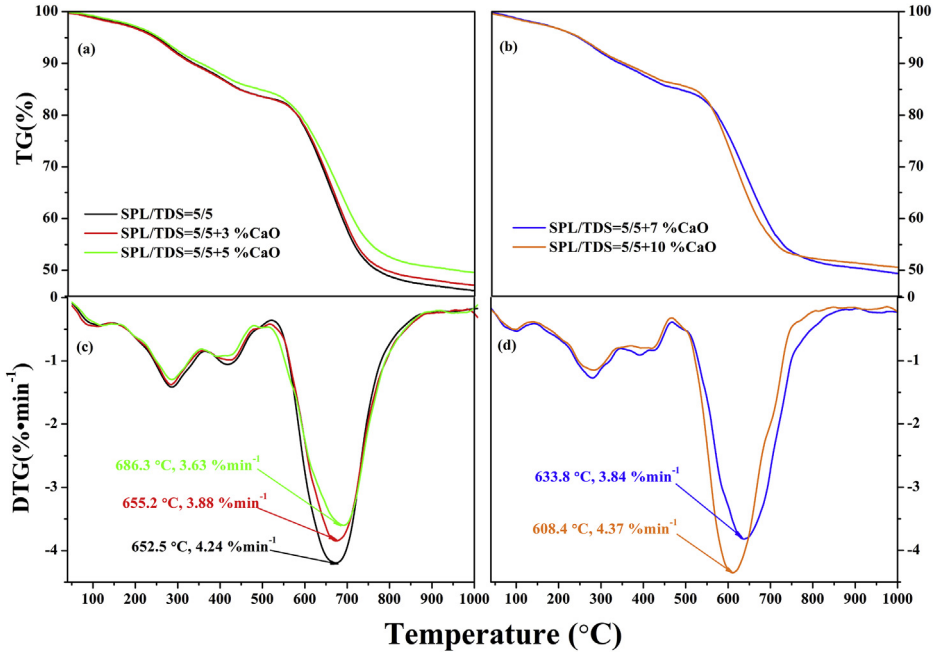

Fig. 4. (a, b) TG and (c, d) DTG curves in response to the addition of the four CaO ratios to the 5/5 blend in the air atmosphere at 20 °C·min^{-1}.

Table 3
Co-combustion parameters in response to the addition of the four CaO ratios to the 5/5 blend in the air atmosphere at 20 °C·min^{-1}.

CaO addition (%)	0	3	5	7	10
Ignition temperature (T_i, °C)	235.3	233.3	237.2	230.2	229.0
Maximum weight loss rate (-R_p, %·min^{-1})	4.24	3.88	3.63	3.84	4.37
Peak temperature (T_p, °C)	652.5	655.2	686.3	633.8	608.4
Average weight loss rate (-R_v, %·min^{-1})	1.13	1.09	1.06	1.07	1.04
Final or burnout temperature (T_f, °C)	868.8	895.6	905.9	905.3	881.1
Final mass (M_f, %)	46.09	48.26	49.57	49.39	50.62
Comprehensive combustion index (CCI, 10^{-8}%^{2}·°C^{-3}·min^{-2})	9.96	8.68	7.55	8.56	9.84

3.6. Residual ashes of co-combustion with CaO addition

The main phases in the ashes were Fe_2O_3, CaF_2, and Na_2SO_4 following the combustion of the 5/5 blends (Fig. 6a). Based on the XRD analyses, most Ca and Na were combined with F^- and S, respectively, during the co-combustion, thus indicating a positive correlation between the mineral changes and the retentions of Ca, Na, S, and F^-. Relative to the mono-combustions of SPL and TDS, the peaks of $CaSO_4$ and NaF disappeared, whereas that of Na_2SO_4 grew stronger during the co-combustion. The S content of TDS enriched the deposit formation with Na_2SO_4. The co-combustion interaction promoted the conversion of $CaSO_4$ and NaF into CaF_2 and Na_2SO_4. The higher thermal stability of CaF_2 than NaF at the high temperatures led to the retention of CaF_2 instead of NaF in the ash. The Na retention in the residual ash with the formation of Na_2SO_4 was attributed to the Na and S-rich contents of the blends. Fe_2O_3 was found to enhance the reactions between SO_2 and the coal minerals, and thus, the S retention capacity of coal ash (Liu et al., 2016).

S, Na, Al, Si, and Fe increased at 1000 °C (Fig. 6c). The retention of alkali metals was shown to rise with the increased temperature (Wei et al., 2018). This may be due to the high-melting temperature compounds formed by Na reacting with Al and Si. Also, it may be because the gases of sodium compounds were directly deposited on the ash surface (Wei et al., 2018). The pronounced influence of the co-combustion on the elemental formations of the residual ash indicated the strong interaction between the fuels. The effects of the CaO addition on the co-combustion at 1000 °C are based on the XRD spectra for the bulk structures, and the XRF analysis of the chemical elements (Fig. 6b). Fe_2O_3, CaF_2, Na_2SO_4, $NaAlO_2$, and $CaAl_2O_4$ were detected to be the main minerals, with no obviously observed intensity corresponding to $CaSO_4$. This was attributed to the decomposition of $CaSO_4$ at about 900 °C. The intensity of CaF_2 in the residual ash grew with the increased ratio of CaO. The XRF results showed that the proportions of Ca and F^- were consistent with the increased CaO content. The evolutions of Fe, Na, Al, Si, and S followed the similar pattern, with Fe_2O_3 still as the main phase in the ash. The increased CaO decreased the signal of Fe_2O_3 but increased the intensity of CaF_2, Na_2SO_4, and $CaAl_2O_4$. $CaAl_2O_4$ was formed by the reaction of CaO with Al_2O_3 during the co-combustion process ($CaO+Al_2O_3 \rightarrow CaAl_2O_4$) (Benitez-Guerrero et al., 2018). S was promoted to transform into the ash slag with the formation of Na_2SO_4 with the increased CaO. These results pointed to Ca influencing the melting and crystalline processes of Fe and Na during the co-combustion.

3.7. Thermodynamic simulations

3.7.1. Inorganic element distributions

Our predictions applied to the range of 600–1200 °C at an interval of 50 °C. A comparison between SPL (Fig. S1) and TDS (Fig. S2) shows that the phase changes grew complicated at the high temperature. As for SPL, NaF increased at below 1000 °C and further converted into HF(g) NaF(g), $(NaF)_2$(g), and $NaAlF_4$(g) at above 1000 °C. The Na_3AlF_6 decomposition led to HF(g) or $NaAlF_4$(g) with the temperature rise. As for TDS, $CaSO_4$ was formed at the low temperature and decomposed at above 850 °C. The increased SO_2 with the temperature rise resulted from the $CaSO_4$ decomposition. Fe_2O_3 in the ash was recalcitrant with the temperature rise. Na_2SO_4, $NaAlSiO_4$, and Fe_2O_3 were stable in the ash slag with the increased temperature (Fig. S3). The lower $CaSO_4$ phase than CaF_2 in the predictions resulted from the higher chemical activity of F^- than S. Our predictions and conclusions were supported by the XRD and XRF analyses above.

NaF was converted into other inorganic compounds, while NaF(g) was formed at above 1000 °C due to the decomposition of CaF_2 in the theoretical simulations. The CaF_2 decomposition contributed to the formations of HF(g) and NaF(g), while Ca was converted into $Ca_{10}(PO_4)_6F_2$, $CaMgAl_{16}O_{27}$, Ca_3MgSiO_8, $Ca_5P_2SiO_{12}$, $Na_2Ca_3Al_{16}O_{28}$, and $Ca_5HO_{13}P_3$ with the further temperature rise. The decomposition of Na_2SO_4 hardly occurred during the co-combustion, as it can be seen in the XRD results. However, the alkali metal retentions were found to fall with the temperature rise, and Na_2SO_4 decomposition occurred at 884 °C (Li et al., 2016). Na was shown to rise from 900 to 1000 °C during the co-combustion of Zhundong coal and sludge (Qi et al., 2018). Relative to the mono-combustion of SPL, the HF emissions increased. Na existed mainly as Na_2SO_4 and $NaAlSiO_4$. The S content of TDS enabled Na to react with S followed by the reaction of F^- with Ca. Na was not combined with F^- unlike the mon-combustion of SPL.

With the increased CaO ratio (Figs. S4–S7), most of F^- was mainly in the form of CaF_2 and converted to HF(g) and NaF(g) with the increased temperature. The F^- emission was promoted by the high temperature, while the HF emission decreased with the increased CaO. The retention of CaF_2 increased, and the decomposition rate grew slowly with the temperature rise. S existed mainly as Na_2SO_4 at below 1050 °C and as $CaSO_4$ which disappeared at 1000 °C. Na_2SO_4 grew recalcitrant and stable in the slag with the increased CaO.

$CaSO_4$ was not observed with 10% CaO. CaF_2 in the slag was converted into $CaMgAl_{16}O_{27}$, Ca_3MgSiO_8, $Ca_5P_2SiO_{12}$, $Na_2Ca_3Al_{16}O_{28}$, and $Ca_5HO_{13}P_3$ with the temperature rise. SO_2 was released slightly due to the decomposition of Na_2SO_4 at above 1100 °C with 10% CaO. $NaAlSiO_4$ was decomposed with the temperature rise during the co-combustion. These results contrasted with the mono-combustion of SPL. The decreased $NaAlSiO_4$ with the increased CaO may result from the formation of Ca, Si, or Al. $CaFe_4O_7$ was formed with more than 7% CaO at above 1150 °C (Fig. S6). Fe was easily reacted with Ca and converted into $CaFe_2O_4$ at above 800 °C with 10% CaO (Fig. S7). The XRD analysis showed a decreased signal of Fe_2O_3 with 10% CaO (Fig. 6b). The results of the FactSage simulations were in a good agreement with the XRD results of the inorganic phase with the temperature rise and the CaO additions. The simulations well predicted the slagging temperature over the wide range of the blends.

3.7.2. Predom diagrams of Ca–Na–S–F analyses

To further understand the formation mechanisms of CaF_2 and Na_2SO_4, the predom diagrams of Ca–Na–S–F at 750, 850 and 1000 °C were computed under the oxygen partial pressure of

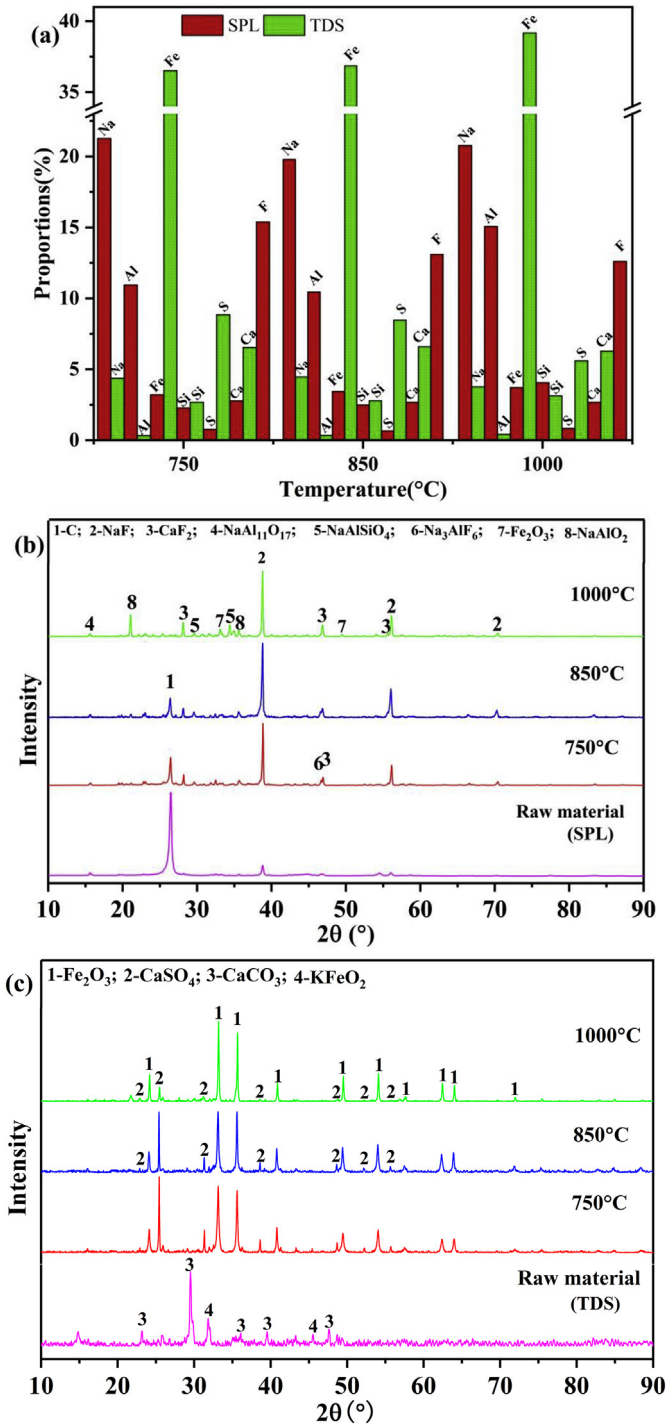

Fig. 5. (a) Chemical matter and ash phases of residual ashes of (b) SPL and (c) TDS mono-combustions.

10^{-10} atm using the thermal simulation software (Fig. 7). The nine regions of inorganic compounds stably occurred under the different SO_2 and F pressures. CaF_2 and Na_2SO_4 were stable at 750 °C between $\log_{10}(P(SO_2)) = 2\log_{10}(P(F)) + 27.52$ and $\log_{10}(P(SO_2)) = 2\log_{10}(P(F)) + 24.97$ ($-8.8 < \log_{10}(P(F)) < -7.1$). The regions of CaF_2 and Na_2SO_4 moved into the high F partial pressure with the increased temperature. With the increased F partial pressure, Na_2SO_4 was converted into NaF, while CaF_2 still existed. With the increased SO_2 partial pressure, CaO was converted into $CaSO_4$.

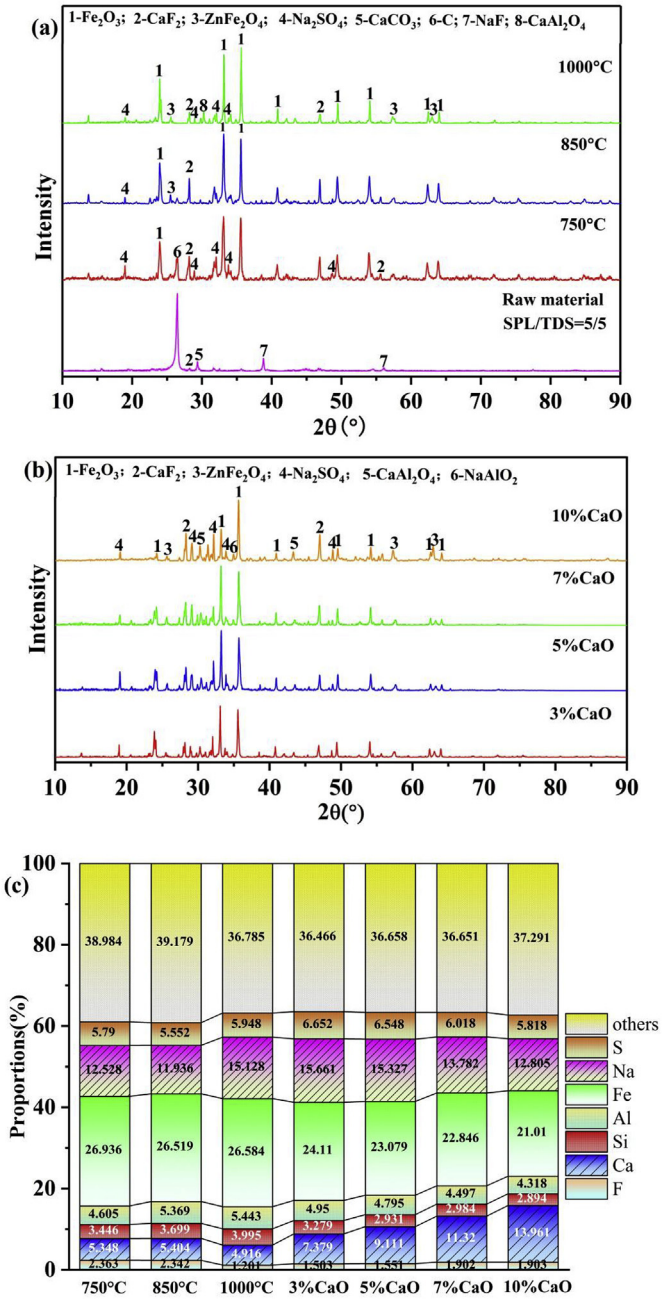

Fig. 6. Ash phases of (a) SPL/TDS (5/5) with (b) the addition of four CaO ratios, and (c) chemical matter in residual ash at 750, 850 and 1000 °C.

3.7.3. Mineral phases according to ternary phase diagrams

The ash characteristics can be theoretically predicted from their major chemical compounds using the ternary diagram. Therefore, the ternary phase diagram systems of $CaO–Na_2O–Al_2O_3$ and $CaO–Fe_2O_3–Al_2O_3$ were computed in this study to obtain the mineral phase transformation of the residual ash. The normalized compositions of SPL, TDS, and their blends (Table 4) were based on the ash compositions of SPL and TDS (Table 1).

A given temperature of the ash composition in the ternary phase diagram systems was indicated by the same color lines in Fig. 8. The points 1 to 7 present the range of SPL, TDS, and their blends. In the $CaO–Na_2O–Al_2O_3$ system (Fig. 8a), the ash composition of SPL and its blends with the addition of CaO was in the $NaAlO_2$ region. The shift of the blend ash to the low temperature with the addition of

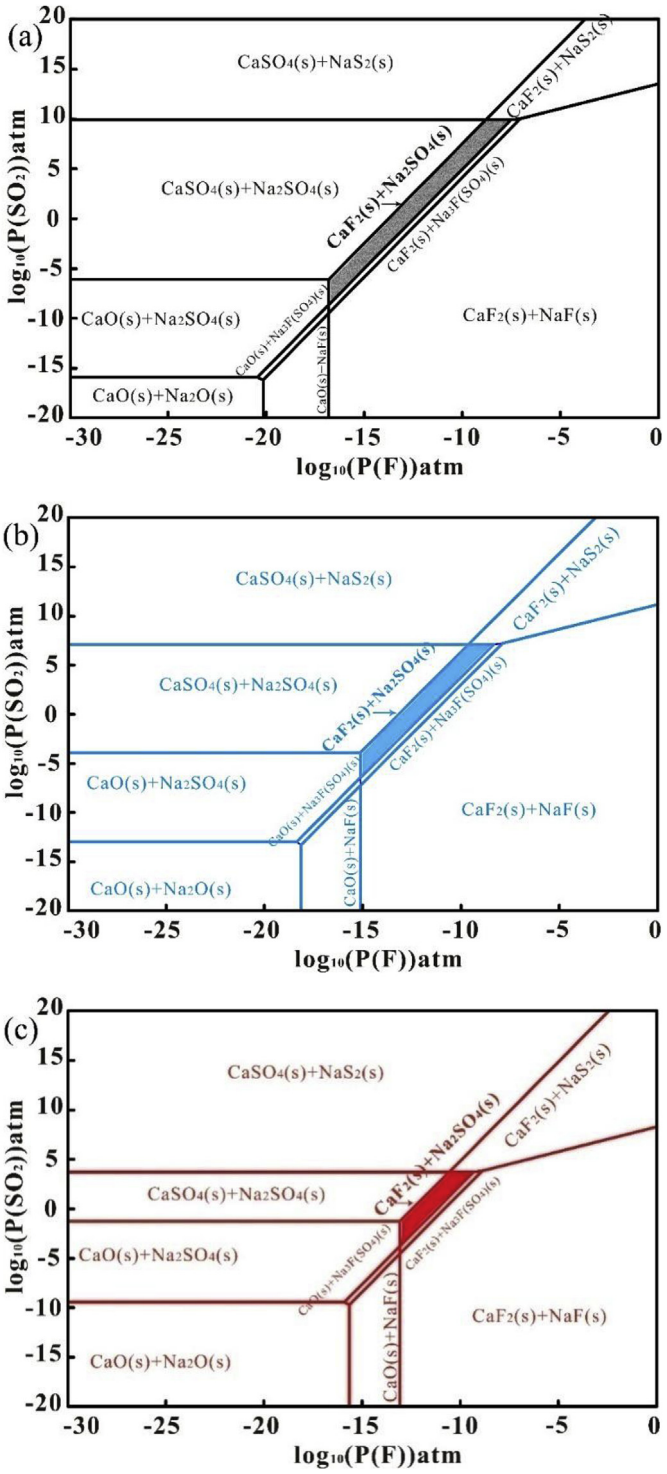

Fig. 7. Predom diagrams of Ca-Na-S-F at (a) 750, (b) 850 and (c) 1000°C.

CaO may be explained by the Na– and Al-rich, and S– and Ca-rich contents of SPL and TDS, respectively. The low-melting temperature ashes were formed due to the interaction among their inner metals, in particular, with the addition of co-solvent lime. Alkali metals were shown to form low-melting temperature ashes such as sodium silicates and sulfates (Qi et al., 2018). However, the ash composition shifted toward the CaO region with more than 5% CaO. The ash melting temperature was the highest with 10% CaO. The high-melting temperature compounds such as CaO species dominated the deposition process.

Table 4
Normalized ash compositions of SPL, TDS, and their blends with the addition of CaO.

	$CaO–Na_2O–Al_2O_3$ system			$CaO–Fe_2O_3–Al_2O_3$ system		
	CaO (%)	Na_2O (%)	Al_2O_3 (%)	CaO (%)	Fe_2O_3 (%)	Al_2O_3 (%)
SPL	5.79	56.66	37.55	11.50	13.96	74.54
TDS	56.42	38.83	4.75	13.33	85.54	1.13
5/5	22.44	50.80	26.76	12.98	71.55	15.47
5/5 + 3% CaO	35.17	42.46	22.37	22.22	63.95	13.83
5/5 + 5% CaO	42.55	37.63	19.82	27.62	59.51	12.87
5/5 + 7% CaO	48.75	33.57	17.68	32.51	55.49	12.00
5/5 + 10% CaO	55.39	29.21	15.40	39.02	50.13	10.85

In the ternary phase system of $CaO–Fe_2O_3–Al_2O_3$ (Fig. 8b), the ashes of the blends and TDS were in the Fe_2O_3 region and moved into the low temperature with the increased CaO. The most stable phase of the 5/5 + 10% CaO blend was on the boundaries of the $CaFe_2O_4$ and $Ca_2Fe_2O_5$ regions. CaO and Fe_2O_3 in the blends produced an ash composition in the hematite region of low temperature for the ternary phase system of $CaO–Fe_2O_3–Al_2O_3$.

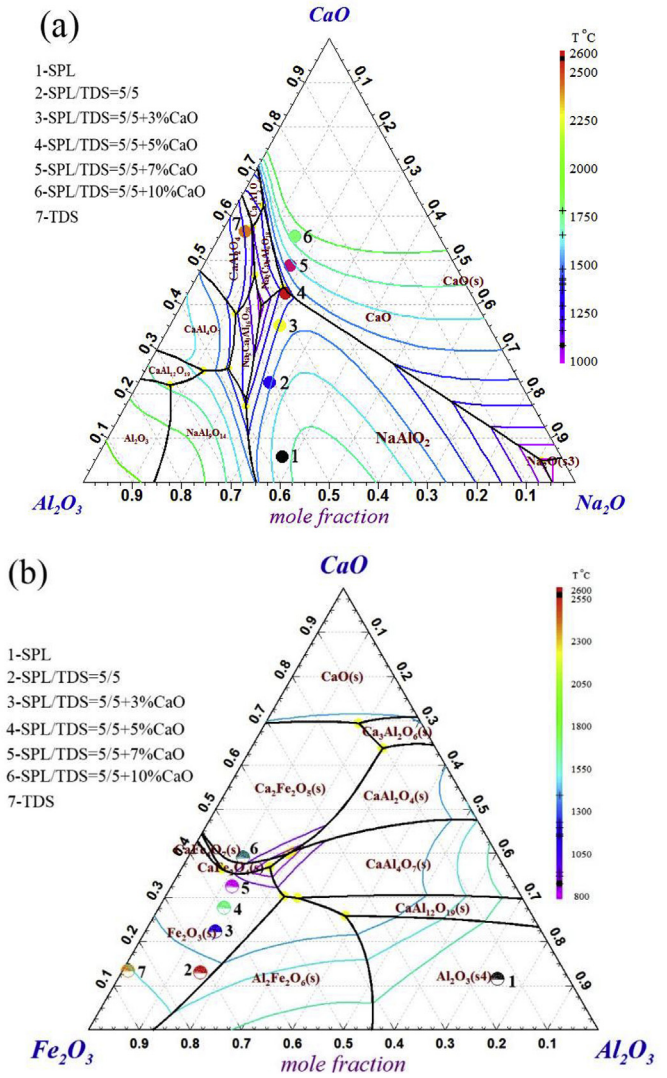

Fig. 8. Ternary phase diagrams of (a) $CaO–Na_2O–Al_2O_3$ and (b) $CaO–Fe_2O_3–Al_2O_3$ systems.

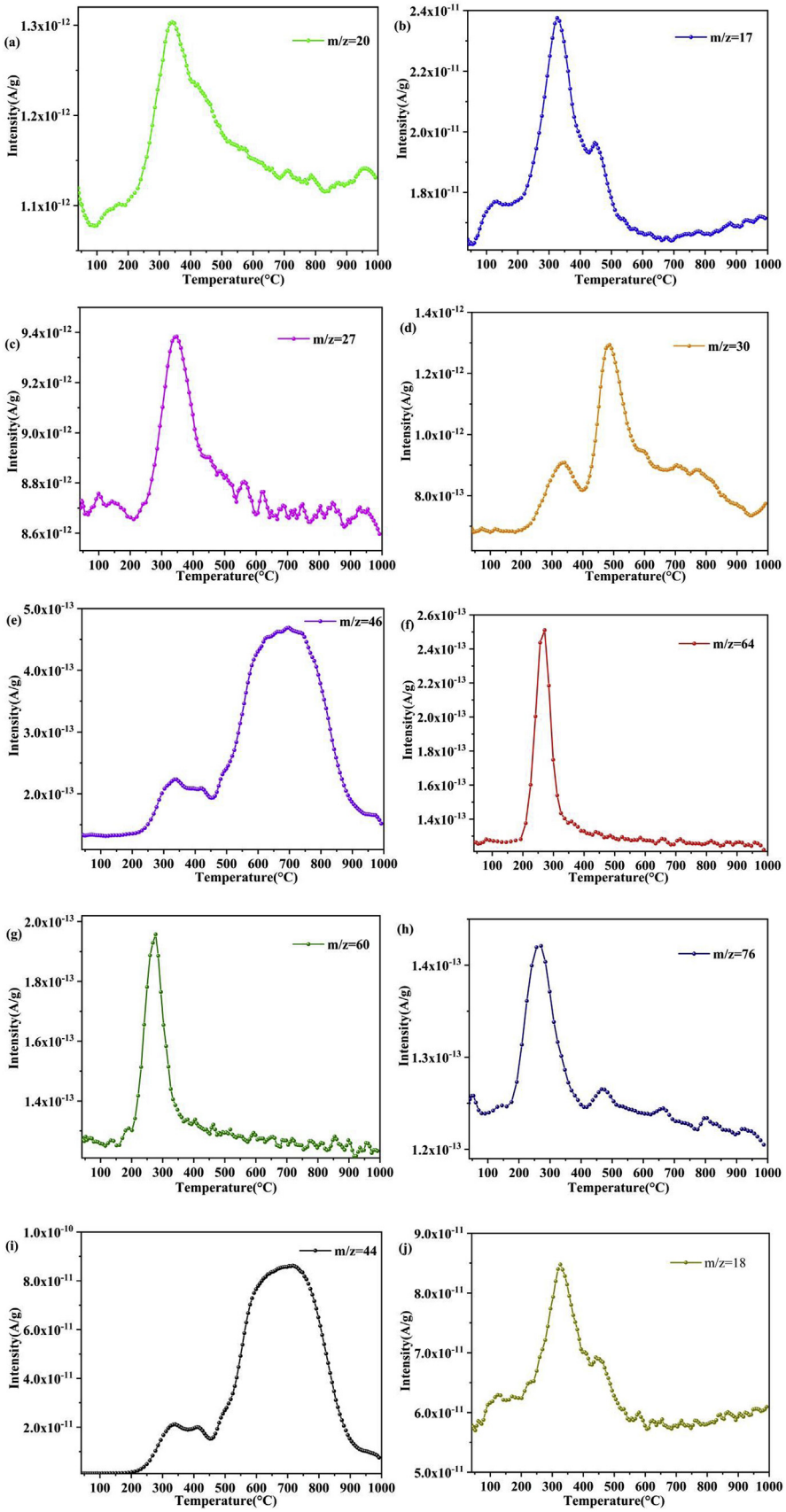

Fig. 9. Changes in gas evolutions from the co-combustion of the 5/5 + 10% CaO blend as a function of temperature in the air atmosphere at 20 °C min^{-1}.

3.8. TG-MS analyses of gas products

The TG-MS analyses were used to achieve a real-time and sensitive detection of flue gases released from the co-combustion of the 5/5 + 10% CaO blend. The main gases included NH_3 ($m/z = 17$), H_2O ($m/z = 18$), HF ($m/z = 20$), HCN ($m/z = 27$), NO ($m/z = 30$), CO_2 ($m/z = 44$), NO_2 ($m/z = 46$), COS ($m/z = 60$), SO_2 ($m/z = 64$), and CS_2 ($m/z = 76$). It should be noted that some ions may refer to different compounds just as ions with $m/z = 44$ are related to CO_2 or N_2O evolution. The release behaviors of typical gas products are given in Fig. 9. For example, the profiles of HF evolution did not significantly change at above 700 °C, while its signal intensity rose dramatically at above 200 °C and peaked at 340 °C (Fig. 9a). Some parts of F^- formed CaF_2 in the residual ash as shown in the above XRD analysis.

NH_3 intensity increased sharply in the range of 200–326 °C during the co-combustion (Fig. 9b–e). The intensity curves of HCN and NH_3 emissions as the main precursors of NO_x emissions were similar (Wang et al., 2018b). NO_x emissions were also related to the decomposition of proteins and aliphatic compounds in TDS. A weak signal peak of NO was observed at 333 °C, and it peaked at 487 °C at the same time as did NO_2. The maximum intensity peak of NO_2 emission occurred at 697 °C from the decomposition of fixed carbon which pointed to its slow formation. This suggested that N-containing compounds were adsorbed by char which generated NO_x emissions when oxidized (Huang et al., 2018). At the low temperatures, NO_2 emission rose according to the following reaction: $NO+O_2 = NO_2+O$ and was reported to depend on the presence of NO (Benajes et al., 2014). NH_3, HCN, NO, and NO_2 were responsible for the large amount of N-containing gases evolved in the co-combustion.

S was released quickly mainly in the forms of SO_2, CS_2, and COS whose behaviors were found to be similar (Fig. 9f–h). The intensity of SO_2 increased at 200 °C, decreased dramatically between 271 and 400 °C and did not change at above 400 °C. The decomposition of aromatic S, FeS_2, or $FeSO_4$ in TDS was shown to account for most of SO_2 emissions (Liu et al., 2018b; Wang et al., 2018b). The main stage of the S release corresponded to the first DTG peak of the organic matter decomposition of the 5/5 + 10% CaO blend. Parts of S mainly formed Na_2SO_4 in the residual ash as shown in the above XRD analyses (Fig. 6b), and the thermal simulations (Figs. S1–S7).

With the adequate O_2 level, hydrocarbons were completely converted into H_2O and CO_2. The CO_2 emission mainly occurred between 450 and 900 °C in the co-combustion stage of fixed carbon (Fig. 9i). The two weak relative intensities observed at 340 and 410 °C were related to the decomposition of organic compounds in TDS. The H_2O evolution occurred slight at 137 °C, peaked at 326 °C due to the decomposition of hydrocarbons and had a weak peak at 450 °C due to the decomposition of aromatic compounds (Fig. 9j).

4. Conclusion

From the (co-)combustion behaviors of SPL and TDS, and their responses to the additions of CaO, the following main conclusions were derived:

(1) The increased comprehensive combustion performance exhibited a stronger interaction with the increased SPL during the co-combustion than the mono-combustion. CaO promoted the co-combustion of fixed carbon with more than 5% CaO.
(2) The interaction effect of the co-combustion was attributed to the combined mechanisms of F^- and S. Ash consisted mainly of CaF_2 and Na_2SO_4 in the co-combustion but of NaF and $CaSO_4$ in the mono-combustions. The increased CaO strengthened the intensity of $CaAl_2O_4$, CaF_2, and Na_2SO_4 but weakened the intensity of Fe_2O_3.
(3) The CaO addition adversely affected the F^- volatilization increasing the F^- content of the ash. The thermodynamic simulations showed the increased CaF_2 with 10% CaO.
(4) The CaO addition changed the most stable phase in the ternary phase system of $CaO–Na_2O–Al_2O_3$ from $NaAlO_2$ to CaO. The melting temperature was higher with more than 7% CaO. The ash-melting temperature moved towards the lower temperature with the shift from Fe_2O_3 to $CaFe_2O_4$ and to $Ca_2Fe_2O_5$ in the ternary phase system of $CaO–Fe_2O_3–Al_2O_3$.
(5) HF, SO_2, COS, CS_2, H_2O, NH_3, HCN, and NO were emitted at < 400 °C during the co-combustion. NO_2 and CO_2 were released in the range of 450–900 °C.

Acknowledgements

This work was financially supported by the National Natural Science Foundation of China (No.51608129), and the Science and Technology Planning Project of Guangdong Province, China (No.2016A050502059, 2018A050506046 and 2019B020208017) and Natural Science Foundation of Guangdong Province of China (2017A030313261).

Appendix A. Supplementary data

Supplementary data to this article can be found online at https://doi.org/10.1016/j.jclepro.2019.03.208.

References

Allen, D., Hayhurst, A.N., 2015. The effect of CaO on emissions of nitric oxide from a fluidised bed combustor. Fuel 158, 898–907.
An, C., Yang, S., Huang, G., Zhao, S., Zhang, P., Yao, Y., 2016. Removal of sulfonated humic acid from aqueous phase by modified coal fly ash waste: equilibrium and kinetic adsorption studies. Fuel 165, 264–271.
Benajes, J., López, J.J., Novella, R., Redón, P., 2014. Comprehensive modeling study analyzing the insights of the NO–NO_2 conversion process in current diesel engines. Energy Convers. Manag. 84, 691–700.
Benitez-Guerrero, M., Valverde, J.M., Sanchez-Jimenez, P.E., Perejon, A., Perez-Maqueda, L.A., 2018. Calcium-Looping performance of mechanically modified Al_2O_3-CaO composites for energy storage and CO_2 capture. Chem. Eng. J. 334, 2343–2355.
Birry, L., Leclerc, S., Poirier, S., 2016. The LCL&L Process: A Sustainable Solution for the Treatment and Recycling of Spent Potlining, Light Metals, pp. 467–471.
Chi, C., Li, Y., Ma, X., Duan, L., 2017. CO_2 capture performance of CaO modified with by-product of biodiesel at calcium looping conditions. Chem. Eng. J. 326, 378–388.
Cieślik, B.M., Namieśnik, J., Konieczka, P., 2015. Review of sewage sludge management: standards, regulations and analytical methods. J. Clean. Prod. 90, 1–15.
Courbariaux, Y., Chaouki, J., Guy, C., 2004. Update on spent potliners treatments kinetics of cyanides destruction at high temperature. Ind. Eng. Chem. Res. 43, 5828–5837.
Fan, Y., Yu, Z., Fang, S., Lin, Y., Lin, Y., Liao, Y., Ma, X., 2016. Investigation on the co-combustion of oil shale and municipal solid waste by using thermogravimetric analysis. Energy Convers. Manag. 117, 367–374.
Fernández, J.R., Abanades, J.C., 2016. CO_2 capture from the calcination of $CaCO_3$ using iron oxide as heat carrier. J. Clean. Prod. 112, 1211–1217.
Gao, L., Mostaghel, S., Ray, S., Chattopadyay, K., 2016. Using SPL (spent pot-lining) as an alternative fuel in metallurgical furnaces. Metall. Mater. Trans. E. 3, 179–188.
Guo, F., Zhong, Z., 2018a. Co-combustion of anthracite coal and wood pellets: thermodynamic analysis, combustion efficiency, pollutant emissions and ash slagging. Environ. Pollut. 239, 21–29.
Guo, F., Zhong, Z., 2018b. Optimization of the co-combustion of coal and composite biomass pellets. J. Clean. Prod. 185, 399–407.
Hao, R., Zhang, Z., Zeng, Q., Mao, Y., He, H., Mao, X., Yang, F., Zhao, Y., 2018b. Synergistic behaviors of anthracite and dried sawdust sludge during their co-combustion: conversion ratio, micromorphology variation and constituents evolutions. Energy 153, 776–787.
Hao, Z., Yang, B., Jahng, D., 2018a. Combustion characteristics of biodried sewage sludge. Waste Manag. 72, 296–305.
Hasanbeigi, Ali, Lynn, P., 2012. A review of energy use and energy efficiency technologies for the textile industry. Renew. Sustain. Energy Rev. 16, 3648–3665.
Hu, S., Ma, X., Lin, Y., Yu, Z., Fang, S., 2015. Thermogravimetric analysis of the co-combustion of paper mill sludge and municipal solid waste. Energy Convers.

Manag. 99, 112–118.
Huang, J., Liu, J., Kuo, J., Xie, W., Zhang, X., Chang, K., Buyukada, M., Evrendilek, F., 2019. Kinetics, thermodynamics, gas evolution and empirical optimization of (co-)combustion performances of spent mushroom substrate and textile dyeing sludge. Bioresour. Technol. 280, 313–324.
Huang, J., Liu, J., Chen, J., Xie, W., Kuo, J., Lu, X., Chang, K., Wen, S., Sun, G., Cai, H., Buyukada, M., Evrendilek, F., 2018. Combustion behaviors of spent mushroom substrate using TG-MS and TG-FTIR: thermal conversion, kinetic, thermodynamic and emission analyses. Bioresour. Technol. 266, 389–397.
Huang, L., Liu, J., He, Y., Sun, S., Chen, J., Sun, J., Chang, K., Kuo, J., Ning, X., 2016. Thermodynamics and kinetics parameters of co-combustion between sewage sludge and water hyacinth in CO_2/O_2 atmosphere as biomass to solid biofuel. Bioresour. Technol. 218, 631–642.
Kijo-Kleczkowska, A., Środa, K., Kosowska-Golachowska, M., Musiał, T., Wolski, K., 2016. Experimental research of sewage sludge with coal and biomass co-combustion, in pellet form. Waste Manag. 53, 165–181.
Li, G., Wang, C.A., Yan, Y., Jin, X., Liu, Y., Che, D., 2016. Release and transformation of sodium during combustion of Zhundong coals. J. Energy Inst. 89, 48–56.
Li, N., Xie, G., Wang, Z.X., Hou, Y.Q., Li, R.X., 2014. Recycle of spent potlining with low carbon grade by floatation. Adv. Mater. Res. 881–883, 1660–1664.
Li, W., Chen, X., 2010. Development Status of Processing Technology for Spent Potlining in China. Light Metals. Springer International Publishing, Cham, pp. 1064–1066.
Li, X., Miao, W., Lv, Y., Wang, Y., Gao, C., Jiang, D., 2018. TGA-FTIR investigation on the co-combustion characteristics of heavy oil fly ash and municipal sewage sludge. Thermochim. Acta 666, 1–9.
Liang, C.Z., Sun, S.P., Li, F.Y., Ong, Y.K., Chung, T.S., 2014. Treatment of highly concentrated wastewater containing multiple synthetic dyes by a combined process of coagulation/flocculation and nanofiltration. J. Membr. Sci. 469, 306–315.
Liu, J., Zeng, J., Sun, S., Huang, S., Kuo, J., Chen, N., 2016. Combined effects of $FeCl_3$ and CaO conditioning on SO_2 , HCl and heavy metals emissions during the DDSS incineration. Chem. Eng. J. 299, 449–458.
Liu, J., Zhuo, Z., Xie, W., Kuo, J., Lu, X., Buyukada, M., Evrendilek, F., 2018b. Interaction effects of chlorine and phosphorus on thermochemical behaviors of heavy metals during incineration of sulfur-rich textile dyeing sludge. Chem. Eng. J. 351, 897–911.
Liu, X., Luo, Z., Yu, C., 2018a. Effect of limestone on the emission of NO during petroleum coke combustion. Fuel 224, 1–9.
Moço, A., Costa, M., Casaca, C., 2018. Ash deposit formation during the combustion of pulverized grape pomace in a drop tube furnace. Energy Convers. Manag. 169, 383–389.
Namkung, H., Lee, Y.J., Park, J.H., Song, G.S., Choi, J.W., Choi, Y.C., Park, S.J., Kim, J.G., 2018. Blending effect of sewage sludge and woody biomass into coal on combustion and ash agglomeration behavior. Fuel 225, 266–276.
Ning, X.A., Lin, M.Q., Shen, L.Z., Zhang, J.H., Wang, J.Y., Wang, Y.J., Yang, Z.Y., Liu, J.Y., 2014. Levels, composition profiles and risk assessment of polycyclic aromatic hydrocarbons (PAHs) in sludge from ten textile dyeing plants. Environ. Res. 132, 112–118.
Niu, X., Shen, L., Gu, H., Jiang, S., Xiao, J., 2015. Characteristics of hematite and fly ash during chemical looping combustion of sewage sludge. Chem. Eng. J. 268, 236–244.
Okoye, F.N., Prakash, S., Singh, N.B., 2017. Durability of fly ash based geopolymer concrete in the presence of silica fume. J. Clean. Prod. 149, 1062–1067.
Ospina, G., Hassan, M.I., 2017. Spent pot lining characterization framework. JOM (J. Occup. Med.) 69, 1639–1645.
Qi, X., Song, G., Song, W., Yang, S., Lu, Q., 2018. Combustion performance and slagging characteristics during co-combustion of Zhundong coal and sludge. J. Energy Inst. 91, 397–410.
Sun, G., Zhang, G., Liu, J., Xie, W., Kuo, J., Lu, X., Buyukada, M., Evrendilek, F., Sun, S., 2019. Thermogravimetric and mass-spectrometric analyses of combustion of spent potlining under N_2/O_2 and CO_2/O_2 atmospheres. Waste Manag. 87, 237–249.
Tian, L., Yang, W., Chen, Z., Wang, X., Yang, H., Chen, H., 2016. Sulfur behavior during coal combustion in oxy-fuel circulating fluidized bed condition by using TG-FTIR. J. Energy Inst. 89, 264–270.
Wang, C., Li, G., Du, Y., Yan, Y., Li, H., Che, D., 2018c. Ash deposition and sodium migration behaviors during combustion of Zhundong coals in a drop tube furnace. J. Energy Inst. 91, 251–261.
Wang, R., Zhao, Z., Qiu, L., Liu, J., 2017. Experimental investigation of synergistic behaviors of lignite and wasted activated sludge during their co-combustion. Fuel Process. Technol. 156, 271–279.
Wang, S., Shan, R., Wang, Y., Lu, L., Yuan, H., 2019. Synthesis of calcium materials in biochar matrix as a highly stable catalyst for biodiesel production. Renew. Energy 130, 41–49.
Wang, Z., Gong, Z., Wang, Z., Fang, P., Han, D., 2018b. A TG-MS study on the coupled pyrolysis and combustion of oil sludge. Thermochim. Acta 663, 137–144.
Wang, Z., Hong, C., Xing, Y., Li, Y., Feng, L., Jia, M., 2018a. Combustion behaviors and kinetics of sewage sludge blended with pulverized coal: with and without catalysts. Waste Manag. 74, 288–296.
Wei, B., Tan, H., Wang, X., Ruan, R., Hu, Z., Wang, Y., 2018. Investigation on ash deposition characteristics during Zhundong coal combustion. J. Energy Inst. 91, 33–42.
Xiao, J., Yuan, J., Tian, Z., Yang, K., Yao, Z., Yu, B., Zhang, L., 2018. Comparison of ultrasound-assisted and traditional caustic leaching of spent cathode carbon (SCC) from aluminum electrolysis. Ultrason. Sonochem. 40, 21–29.
Xie, C., Liu, J., Zhang, X., Xie, W., Sun, J., Chang, K., Kuo, J., Xie, W., Liu, C., Sun, S., Buyukada, M., Evrendilek, F., 2018a. Co-combustion thermal conversion characteristics of textile dyeing sludge and pomelo peel using TGA and artificial neural networks. Appl. Energy 212, 786–795.
Xie, W., Huang, J., Liu, J., Zhao, Y., Chang, K., Kuo, J., He, Y., Sun, J., Zheng, L., Xie, W., Sun, S., Buyukada, M., Evrendilek, F., 2018b. Assessing thermal behaviors and kinetics of (co-)combustion of textile dyeing sludge and sugarcane bagasse. Appl. Therm. Eng. 131, 874–883.
Xie, Z., Ma, X., 2013. The thermal behaviour of the co-combustion between paper sludge and rice straw. Bioresour. Technol. 146, 611–618.
Xing, P., Darvell, L.I., Jones, J.M., Ma, L., Pourkashanian, M., Szuhánszki, J., Williams, A., 2018. The use of equilibrium thermodynamic models for the prediction of inorganic phase changes in the co-firing of wheat straw with El Cerrejon coal. J. Energy Inst. https://doi.org/10.1016/j.joei.2018.02.003.
Zhang, G., Hai, J., Ren, M., Zhang, S., Cheng, J., Yang, Z., 2013. Emission, mass balance, and distribution characteristics of PCDD/Fs and heavy metals during cocombustion of sewage sludge and coal in power plants. Environ. Sci. Technol. 47, 2123–2130.
Zhang, Q., Liu, H., Zhang, X., Xing, H., Hu, H., Yao, H., 2017. Novel utilization of conditioner CaO for gas pollutants control during co-combustion of sludge and coal. Fuel 206, 541–545.
Zhuo, Z., Liu, J., Sun, S., Sun, J., Kuo, J., Chang, K., Fu, J., Wang, Y., 2017. Thermogravimetric characteristics of textile dyeing sludge, coal and their blend in N_2/O_2 and CO_2/O_2 atmospheres. Appl. Therm. Eng. 111, 87–94.